26. These are 11.92 km/s for fcc and 11.73 km/s for hcp.
27. We focus on differential travel times because these are least contaminated by other potential sources of velocity anisotropy. The abbreviations PKP_{BC} and PKP_{AB} refer to ray paths that are shallower than *PKIKP* so that they do not enter the inner core; PKP_{DF} is synonymous with *PKIKP*. Anomalous BC − DF (*3, 7*) observations are centered near $\Delta = 150°$ ($t = 124$ s); anomalous AB − DF observations (*8*) are clustered near $\Delta = 175°$ ($t = 230$ s). To ensure an even coverage in ξ for both BC − DF data sets, we used the binned data of Creager (*3*). The BC − DF and AB − DF travel times are corrected for the ellipticity of Earth.
28. The AB − DF travel times are likely biased by mantle structure so that they are larger (by approximately 0.5 s) than what inner core structure alone would produce (*8*).
29. S_{eq} is polarized in the equatorial plane, S_{me} in the meridional plane defined by the propagation direction and the rotation axis. In the hcp forward model of the inner core, these polarizations correspond to the (001) and (010) crystallographic planes, respectively.
30. This is a converted phase that travels as an *S* wave only in the inner core.
31. The S_{eq} and S_{me} travel times were computed for $\xi = 45°$ and $\Delta = 260°$ in the IASP91 model [B. N. L. Kennett and E. R. Engdahl, *Geophys. J. Int.* **105**, 429 (1991)] with a code provided by C. W. Wicks.
32. C. M. Sayers, *Geophys. J. Int.* **103**, 285 (1990).
33. ______, *Geophys. Res. Lett.* **16**, 267 (1989).
34. The effect of nickel, which is thought to be the most abundant alloying constituent, is probably small. The equation of state of iron-nickel alloys at core pressures is known to be virtually independent of composition up to 20% nickel (*15*). The light element that is present in the outer core (possibly O, S, Si, H, or C) may exist in the inner core as well. The effect of this light element is expected to be small because seismological observations constrain its abundance in the inner core to less than a few percent (*14*).
35. R. Hollerbach and C. A. Jones, *Nature* **365**, 541 (1993).
36. Paleomagnetic data indicate that the inner core was formed at least 4 billion years ago. If we assume a linear growth rate, the outermost 300 km, to which the BC − DF observations are most sensitive, would have formed in 1 billion years. Recent observations, which indicate that the outermost 50 to 100 km of the outer core is isotropic [X. Song and D. V. Helmberger, *J. Geophys. Res.*, in press; P. Shearer, *ibid.* **99**, 19647 (1994)], suggest that these most recently formed regions may not have had sufficient time to develop anisotropy through recrystallization.
37. This mechanism is discussed in F. D. Stacey, *Physics of the Earth* (Brookfield, Auckland, New Zealand, 1992), pp. 210–211.
38. We thank K. Creager (*3*) and X. Song (*7*) for providing their travel time data in digital form, C. W. Wicks for the code used to calculate *PKJKP* travel times, and U. Christensen, R. Jeanloz, P. Shearer, X. Song, J. Tromp, and C. Wicks for comments on the manuscript and helpful discussions. Supported by the National Science Foundation under grant EAS-9305060. L.P.S. was also supported by an Alexander von Humboldt Foundation fellowship.

9 November 1994; accepted 19 January 1995

Biogeological Mineralization in Deep-Sea Hydrothermal Deposits

Terri L. Cook* and Debra S. Stakes

Oriented drill cores retrieved from active massive sulfide edifices at the Endeavour Segment of the Juan de Fuca Ridge contain an abundance of fossilized tube structures associated with vestimentiferan and annelid worms. The petrological evolution of these biogeological structures and their presence deep inside the edifice walls demonstrate that an initial, worm-mediated texture directly affects the subsequent steps of inorganic precipitation, wall infilling, and outward growth of these black smoker deposits. The presence of fossilized structures in hydrothermal discharge sites that are 2 kilometers apart and their similarity to structures observed in other modern and ancient deposits suggest that these biogeological processes are general phenomena.

Although the presence of biological structures or their remains in northeast Pacific mid-ocean ridge sulfide deposits has been commonly reported (*1–7*), an understanding of both the biogeological interactions and the processes of hydrothermal mineralization has been difficult to obtain because of a lack of oriented samples encompassing the outward growth of the deposits. Here we describe worm-derived textures in oriented cores drilled into the main bodies of large black smoker edifices (*4, 8*). These textures are composed of distinctive, concentrically layered worm tube structures generally surrounded by massive, wall-infilling crystals. Similar tube structures have been described as cross sections of fossilized chitinous worm tubes (*6*), and the concentric mineralogical layering has been observed in many sulfide deposits (*2–6, 9, 10*). Five petrological sequences observed in the drill cores show that the development of this concentric layering is initiated by the presence of worms and may also be controlled by microflora before inorganic reactions dominate the final stages of its development. Preservation of the tube structures after abandonment or decay of the organic matter provides ample fluid conduits that influence the edifices' thermal and chemical gradients and porosity (*5, 11*), directly affecting lateral growth.

The Endeavour sulfide zone encompasses two major active hydrothermal areas: the High Rise Site (HRS) (8) and the Main Field Site (MFS) (*2, 12*) (Fig. 1). The largest, northernmost structures in both fields are characterized by four venting types: small (i) black and (ii) white smoker chimneys atop the edifices, (iii) high-temperature fluids pooled beneath protruding, ledge-type "flanges," and (iv) diffuse flow through the flanges (*8, 12*).

We focus on three drill cores collected in 1991. All three were drilled from active edifices (*4*), although the sampled areas were inactive and biologically barren. (i) Core 2466 was drilled from the base of the Hulk edifice in the northern MFS (*12*) (Fig. 1). The core is divided into six pieces totaling 27 cm in length and is composed of massive Fe and Zn sulfides (Table 1). Tube structures are present throughout the core and are associated with barite in pieces A and B. (ii) Core 2464 was drilled from Godzilla, an edifice in the northernmost HRS (Fig. 1). The core was drilled into a flange scar (flange attachment point characterized by remnant horizontal layering) halfway up the 45-m-high structure (*8*). Core 2464 is divided into seven pieces totaling 30 cm. The dominant mineral phase varies between pieces in this core, which is unusual for samples in this study (Table 1). Numerous fossilized tube structures up to 1 cm wide are observed in all but the innermost piece. The structures are associated with barite in piece A. (iii) Core 2461 is from the base of Boardwalk, another large structure at the northern HRS (*8*). This core is divided into seven pieces totaling 29 cm and is dominantly composed of Fe and Zn sulfides and amorphous silica (Table 1). Barite is present throughout the core and is associated with abundant tube structures in the interior end and center.

Our criteria for the identification of worm tube structures are based on examples from modern and ancient deposits (*1–6, 9, 10*). Most Endeavour sulfide samples contain large numbers of living alvinellid polychaete and vestimentiferan worms, which occupy up to 25% of the total sample volume. Poorly consolidated chimney material commonly fell apart when the worms were removed. The oval layering that we describe as worm tube structures is the only space in the outer sulfide wall that can accommodate the abundance of living worms covering the active edifices (*12–14*).

The textures of the tube structures and commonly their mineralogy differ from those of the wall matrix material. Most thin sections contain 20 to 35% tube structures,

---

T. L. Cook, Monterey Bay Aquarium Research Institute, 160 Central Avenue, Pacific Grove, CA 93950, and Earth Sciences Board, University of California, Santa Cruz, CA 95064, USA.
D. S. Stakes, Monterey Bay Aquarium Research Institute, 160 Central Avenue, Pacific Grove, CA 93950, USA.

*To whom correspondence should be addressed at the Monterey Bay Aquarium Research Institute.

but individual sections contain between 0 and 60%. On average, worm tube structures account for about 20% of the porosity in the thin sections, although this figure rises considerably when sections with infilled tube structures are excluded. In the extreme case, the structures account for 60% of a section's porosity.

The evolution of the tube structures' layering has been inferred from five petrological sequences observed in the drill cores. These sequences have been sequentially numbered I through V on the basis of their structural and compositional evolution. The sequences' mineralogical compositions represent an evolving progression from relatively low-temperature (sequence I) to high-temperature (sequences IV and V) phases.

Sequence I is characterized by a thin (<0.1 mm) layer of barite ubiquitously coated with clear amorphous silica (Fig. 2A). The minerals define an oval-shaped tube structure (0.3 to 0.8 cm in diameter) encircling void space. The porous space between the tube structures is occupied by rare acicular barite laths and minor marcasite.

Fig. 1. Location map of the Endeavour sulfide zone encompassing the principal hydrothermally active areas. Edifices at the MFS and HRS are structurally controlled features associated with intersecting faults presumed to channel the hydrothermal fluids (*8*, *12*). The largest structures are shown with dots and include Godzilla and Boardwalk at the northern HRS (*8*) and Hulk at the northern MFS (*12*). Contour lines indicate depth in meters. Map modified from (*8*).

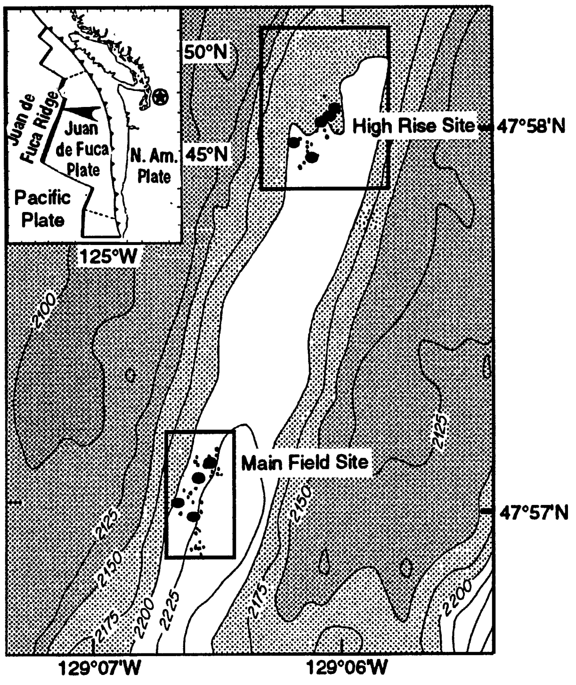

Table 1. Estimated volumetric mineral abundances in cores 2461, 2464, and 2466. The dominant phases are highlighted to show the unusual mineralogical variation in Core 2464. The "A" piece of each core represents the exterior end (seawater-sulfide interface); the "F" and "G" pieces are the interior end. The center of the core refers to the pieces between these ends. Estimates are based on petrographic examination of singly polished thin sections. Mineral identifications and textural interpretations were made with transmitted- and reflected-light petrographic techniques and electron microprobe analyses. Thin sections that include a "V" were oriented vertically with respect to the core ends. Miscellaneous minerals include barite and various Cu-Fe-S phases.

Core	Section	Volume (% of total)						
		FeS_2	ZnS	$CuFeS_2$	Si	PbS	Miscellaneous	Void
2461	A	25	15	<1	**30**		10	20
	A-V	**45**	23	<1	15		2	15
	D	21	15	<1	**40**	<1	4	20
	D-V	19	15	3	**30**		8	25
	F-V	29	9	1	**40**	<1	6	15
2464	A	5	**64**	1	<1		5	25
	A-V	3	**66**	1	2		3	25
	C	17	3	<1	**50**			30
	D-V	15	3	4	**53**			25
	F	**32**	8	5	20			35
	F-V	**48**	4	8	15			25
	G	10	15	**47**	12		1	15
2466	A	**40**	10		30	<1	9	10
	A-V	**35**	<1		25		25	15
	C	**35**	25	<1	25	<1	5	10
	D	**40**	10	<1	35	<1	<1	15
	F	**35**	25	<1	15			25

Sequence II is identified by the first stage of iron sulfide accumulation. A barite + silica structure similar in size and shape to that of sequence I has individual iron sulfide framboids (≤10 μm in diameter) attached to its inside or outside edges. In some structures, the framboids form a thin, discontinuous layer along one or both sides of the barite tube structure (Fig. 2B), whereas in other examples, the framboids are attached to a layer of outwardly (exterior to ring) or inwardly projecting, silica-coated barite laths. Between clustered tube structures, dendritic barite laths, silica, and lesser marcasite are present.

Further iron sulfide accumulation and the absence of barite characterize sequence III, examples of which have been noted in other studies (*3*, *5*, *6*). From exterior to interior, sequence III structures consist of five layers (Fig. 2C). Layer (i) is composed of outwardly-directed iron sulfide lamellae and amorphous silica. Microprobe analyses (Tables 2 and 3) and morphology indicate that feathery, lath-shaped areas now infilled with late-stage silica were previously occupied by barite intergrown with the iron sulfide lamellae. Layer (ii) contains late-stage amorphous silica spherules coating abundant, heterogeneously distributed, unidentified black particulates (≤0.05 mm in diameter). Layer (iii) is a poorly developed pyrite-marcasite layer commonly associated with silica-infilled, lath-shaped areas and intergrown, inwardly radiating iron sulfide lamellae. Layer (iv) is a thin band of black particulates along much of the inner iron sulfide rim. The structures' interiors, forming layer (v), are partially to completely infilled with silica and iron sulfide, plus or minus small quantities of higher temperature minerals (see sequence IV).

Initial marcasite accumulation is observed as small, individual crystals attached only to the iron sulfide framboids (Fig. 2B), whereas further marcasite accumulation is present as colloidal aggregates and both outwardly and inwardly radiating lamellae. The outer layer of iron sulfide [layer (i)] is generally zoned, with an exterior band of marcasite grading into a layer of pyrite next to layer (ii). Layer (ii) is present in the location occupied by barite in sequences I and II. Much of the area between sequence III tube structures is infilled with dendritic iron sulfide crystals.

Sequence IV differs from sequence III by the presence of higher temperature Zn-sulfide and Cu-Fe sulfide minerals in layers (i), (ii), (iii), or (v) (Fig. 2, D and E). In sequence IV, the rings' centers [layer (v)] are infilled with large wurtzite or chalcopyrite (or both) crystals (≤0.5 cm) differing in size and composition from the surrounding wall material (Fig. 2E). Layer (ii) is either no longer observed (Fig. 2E) or is partially filled with small (≤0.1 mm) anhedral wurtzite or pyrite crystals (Fig. 2D). Where layer (v) is predominantly composed of chalcopyrite, no marcasite is observed in the remnant layers of iron sulfide [layers (i) and (iii)]. Examples of sequence IV are nearly identical to examples described from modern vents and from ancient ophiolites (*6*).

Sequence V structures lack all or most of the layers described above (Fig. 2F). These tube structures are not always identifiable and might be considered part of the porous sulfide wall, except that they are occasionally clustered and some contain remnants of concentric layering. Sequence V structures are concentrated toward the interior ends of the cores.

Several observations indicate that these petrological sequences result from worm fossilization. (i) Worms were directly removed from the Endeavour samples. (ii) At Endeavour, workers have observed the sulfide entombment of worms protruding from edifice walls (*15*). (iii) The structures are consistent in size and shape, they are found individually and in clusters, as are live worms, and their size is consistent with the size of worms retrieved from the samples. (iv) Evidence from several studies (*3*, *16*–*18*) indicate that some vent worms promote deposition of the initial barite + amorphous silica assemblage.

Although some workers initially suggested that the concentric layering resulted from episodic variations in fluid flow or composition (*9*), subsequent studies have dismissed this hypothesis because of the rings' consistent appearance and the availability of modern biological samples for comparison (*6*, *10*). Similarly, open-space deposition would not produce concentric rings of consistent size, shape, and composition in such a complex depositional environment.

Evidence that these petrological sequences do represent a temporal progression is derived from each sequence's mineral assemblage and its structural features. Using East Pacific Rise (EPR) fluid compositions from 21°N, Janecky and Seyfried (*19*) and Tivey and McDuff (*20*) have estimated that chalcopyrite precipitates above 325°C, whereas Fe- and Zn-sulfide assemblages are generally deposited at intermediate temperatures. Barite is considered a low-temperature phase (6° to ~60°C) (*3*, *10*, *19*, *20*), although its exact range of thermal stability is unknown. Amorphous silica precipitation results from conductive heat loss and is estimated to occur between 60° and 172°C (*19*, *20*).

The simple composition and shape of sequence I (Fig. 2A), its close association with hydrothermal worms (*3*, *6*, *10*), and biogeochemical studies (*3*, *16*–*18*) all provide evidence that this sequence is a biologically mediated coating covering the worms and the exterior edifice walls.

Framboids are uncommon in the cores except in sequence II tube structures, where they are generally attached to the initial barite layer (Fig. 2B). Because the framboids consistently line the barite structure, they must postdate it, and we therefore conclude that sequence II tube structures are more evolved versions of sequence I tube structures. In addition, the framboids' nearly exclusive attachment to the barite ring suggests that the in situ production of polysulfide species from the barite is an important mechanism for framboid development (*19*, *21*, *22*).

Sequence III is distinguished from sequence II by the habit of iron sulfide precipitation and its intermediate-temperature (iron sulfide–rich and barite-poor) assemblage. In sequence II tube structures, iron

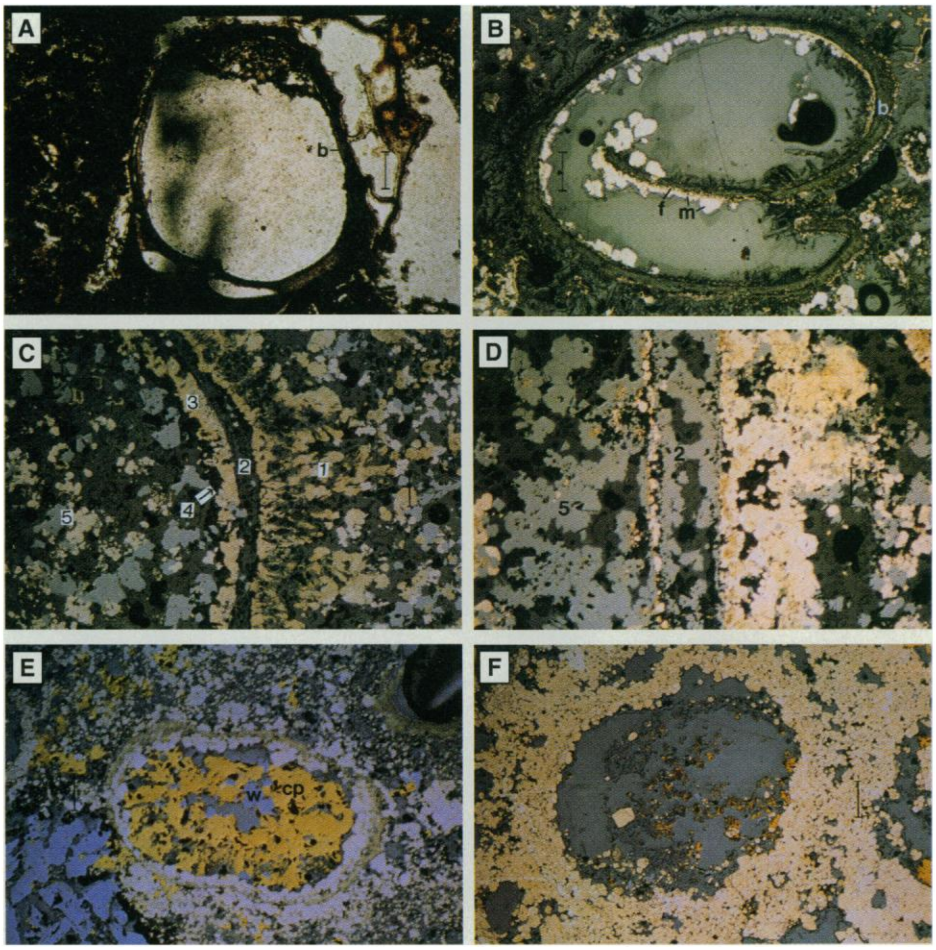

Fig. 2. Photomicrographs depicting the petrographical evolution of worm tube structures in active black smoker sulfide deposits. **(A)** Sequence I: A low-temperature barite tube structure (b) coated with clear, amorphous silica encircling void space (transmitted light; core 2461, section D-V). The scale bar is 0.42 mm. **(B)** Sequence II: Iron sulfide framboids attached to the inner wall of a barite (b) + silica tube structure. The darker yellow framboids (f) form a thin, discontinuous rim and provide a surface for marcasite (m) deposition. The framboids' presence and other geochemical evidence suggest that magnetotactic bacteria may control this transition from sulfate to sulfide deposition (reflected light; core 2466, section A-V). The scale bar is 0.42 mm. **(C)** Sequence III: Close-up picture of the layers characteristic of later-stage tube structures. Layer (i) (1): outwardly radiating, silica-coated iron sulfide lamellae previously intergrown with barite laths. Layer (ii) (2): porous layer containing disseminated black particulates in late-stage amorphous silica. Layer (iii) (3): a poorly developed interior iron sulfide layer. Layer (iv) (4): a discontinuous layer of the unidentified black particulates. Layer (v) (5): the structure's interior partially infilled with silica-coated wurtzite and iron sulfide. Note the particulates scattered through part of layer (i) near the top of the photograph (reflected light; core 2466, section A). Scale bar is 0.21 mm. **(D)** Sequence IV: Close-up picture of wurtzite infilling layers (v) (5) and (ii) (2). Layer (ii) is delineated by iron sulfide framboids and crystals. Note the chalcopyrite disease (2) present on some of the wurtzite (reflected light; core 2466, section C). Scale bar is 0.21 mm. **(E)** Sequence IV: Chalcopyrite (cp) and wurtzite (w) infilling [(layer (v)]. Note the lack of layer (ii), which is now infilled with iron sulfide as a precursor to the structure's disappearance (reflected light; core 2464, section F). Scale bar is 0.83 mm. **(F)** Sequence V: With further infilling and recrystallization, the tubes are eventually erased (reflected light; core 2464, section F). Structure is composed of pyrite; scale bar is 0.42 mm.

sulfide is only present as framboids or as individual marcasite crystals attached to the framboids (Fig. 2B). In sequence III tube structures, iron sulfide is present as lamellae and colloidal aggregates (Fig. 2C). Gradations between these two sequences and the advancement from lower- to intermediate-temperature assemblages provide direct evidence that sequence III tube structures are more evolved versions of sequence II tube structures.

From the incremental nature of the iron sulfide accumulation, we conclude that the framboids provide a nucleation site for further marcasite collection (*23*). Magnetotactic (magnetic mineral–containing) bacteria may provide a basis for framboid formation (*24*), although their origin has been the subject of debate (*24*, *25*). Uranium enrichments measured in EPR chimneys (*26*) have been attributed to worm tube–colonizing bacteria, and a seawater uranium enrichment in core 2464 is associated with the framboids (*22*). These data suggest that microflora may be responsible for the transition from predominantly sulfate to sulfide assemblages by providing a nucleation site for sulfide accumulation.

The presence of massive dendritic sulfide crystals between the tube structures indicates that the space between them was rapidly infilled with massive sulfides as the wall grew around the structures. The onset of layer (v) infilling and the zonation of layer (i) provide evidence that the tube structures affect wall porosity by acting as fluid conduits during this expansion. Because iron sulfide deposition is dominantly controlled by pH and temperature, interaction with high-temperature fluids would cause the marcasite nearest the fluids to invert to pyrite (*27*). Increasing fluid temperatures and evolving fluid compositions also account for the absence of barite in sequence III. The black disseminated material may be remnant organic matter, but its origin is uncertain.

The size of the large crystals in sequence IV suggests that they were deposited in open space (*5*), and their intermediate- to high-temperature compositions reflect a chemical environment increasingly isolated from mixing with seawater (*28*). Continued fluid flow through the tube structures brought the sequence III layers in contact with increasingly hotter fluids, completely inverting the iron sulfide of layers (i) and (iii) to pyrite, recrystallizing or infilling the layers with high-temperature sulfide minerals, and eventually depositing the highest temperature assemblage in layer (v). On the basis of replacement textures (*29*), evidence of continued fluid flow through the structures, and their higher temperature mineral assemblages, we conclude that sequence IV tube structures are more evolved versions of sequence III tube structures. The structures' function as fluid conduits creates large thermal and chemical gradients over millimeter-scale distances in the encroaching sulfide matrix. Similarly, on the basis of the infilling and recrystallization of layers (i), (ii), (iii), and (v) (Fig. 2, D and E) and the disappearance of layer (ii) (Fig. 2E), we conclude that the tube structures are eventually destroyed. Sequence V represents tube structures in the process of being overprinted by this inorganic precipitation during the final stage of their evolution (Fig. 2F).

In EPR chimneys, there is a clear exterior-to-interior mineralogical progression in agreement with a decaying thermal gradient from the chimney's central conduit (*10*, *21*, *28*). In the Endeavour cores, we see a similar gross spatial relationship for the tube structures. The sequences with low-temperature minerals generally occur at the cores' exterior ends, whereas the sequences with high-temperature phases are found toward the interior ends. However, we do not see such a relation in the cores' bulk petrology (Table 1). Given the enormity of the Endeavour edifices and their multiple fluid conduits and flanges, it is not surprising that the cores' mineralogy violates the simple progression described for EPR chimneys (*28*). However, these differences do not alter our model, which is based on the temporal mineralogical progression of the tube structures rather than on spatial mineralogical trends.

The presence of a biological substrate stabilized by barite + amorphous silica cementation may affect flange development by providing a platform on which spires can be constructed (*3*). At the Endeavour Segment, worms are commonly observed extending outward from the upper edifice walls (*15*). During periods of lateral flow (*12*), these outwardly directed fauna could provide sufficient surface area (*17*) and influence the chemical gradients and concentrations (*16*) necessary for mineral deposition and lateral expansion by means of the processes of biomineralization discussed herein.

Table 2. Subset of electron microprobe analyses of biologically-associated sulfides. Analyses were performed on a Cameca SX-50 WDS at the University of California, Davis.

Mineral	Sample	Composition (weight %)									Total
		Zn	As	Si	S	Pb	Ag	Fe	Cu	U	
FeS_2					*Framboids*						
	2464 C		0.06	0.22	53.6			46.0	0.04		99.9
	2464 C	0.04		0.63	52.7		0.12	45.1	0.12		98.7
	2466 A-V	0.12	0.12	0.07	51.0		0.12	43.7	0.10		95.2
					Tube-associated						
	2464 C		0.06	0.87	52.3		0.04	45.6			98.9
	2466 C	0.09	0.14	0.05	53.8	0.06	0.05	46.4			100.6
	2466 D		0.09		54.4	0.04		47.0		0.11	101.6
	2466 F				54.0			47.1	0.07	0.18	101.4
ZnS					*Tube-associated*						
	2466 D	55.2	0.04		33.5		0.07	10.1			98.9

Table 3. Subset of electron microprobe analyses of biologically associated sulfates and amorphous silica. Analyses were performed on a Cameca SX-50 WDS at the University of California, Davis.

Mineral	Sample	Composition (weight %)					Total
		SO_3	SiO_2	CaO	SrO	BaO	
$BaSO_4$			*Tube-associated*				
	2466 A-V	34.2	0.06	0.19	1.43	63.1	99.0
	2466 A-V	34.9	0.04	0.05	0.45	65.2	100.6
Si			*Tube-associated*				
	2466 A-V	0.78	96.1		0.27		97.2

REFERENCES AND NOTES

1. R. A. Koski, I. R. Jonasson, D. C. Kadko, V. K. Smith, F. L. Wong, *J. Geophys. Res.* **99**, 4813 (1994).
2. M. K. Tivey and J. R. Delaney, *Earth Planet. Sci. Lett.* **77**, 303 (1986).
3. M. D. Hannington and S. D. Scott, *Can. Mineral.* **26**, 603 (1988).
4. D. S. Stakes *et al.*, *Eos* **73**, 273 (1992).
5. R. A. Koski, D. A. Clague, E. Oudin, *Geol. Soc. Am. Bull.* **95**, 930 (1984).
6. R. M. Haymon, R. A. Koski, C. Sinclair, *Science* **223**, 1407 (1984).
7. S. K. Juniper, I. R. Jonasson, V. Tunnicliffe, A. J. Southward, *Geology* **20**, 895 (1992).
8. V. Robigou, J. R. Delaney, D. S. Stakes, *Geophys. Res. Lett.* **20**, 1887 (1993).
9. R. Hekinian, M. Fevrier, J. L. Bischoff, P. Picot, W. C. Shanks, *Science* **207**, 1433 (1980).
10. R. M. Haymon and M. Kastner, *Earth Planet. Sci. Lett.* **53**, 363 (1981).
11. M. K. Tivey, in preparation.
12. J. R. Delaney, V. Robigou, R. E. McDuff, M. K. Tivey, *J. Geophys. Res.* **97**, 19663 (1992).
13. Biological reports from the Endeavour Segment confirm that high-temperature sulfide worms, more

moderate-temperature palm worms, and vestimentiferan tube worms are abundant (*12, 14*). The terms "tube" and "tube structure" refer to a structure's shape and do not necessarily indicate that it results from a vestimentiferan tube worm. Because all of the described structures are relict and several types of worms are currently abundant at Endeavour, we are unable to define which worms are associated with the described structures. However, the worms' association with barite, a low-temperature phase (*3, 10*), suggests that low- to intermediate-temperature worms formed these structures.

14. M. Hannington and K. Juniper, *Ridge Res. Rep.* **3**, 38 (1992); V. Tunnicliffe and S. K. Juniper, *Prog. Oceanogr.* **24**, 1 (1990).
15. D. S. Stakes and W. S. Moore, *J. Geophys. Res.* **96**, 21739 (1991).
16. V. Tunnicliffe, S. K. Juniper, M. E. de Burgh, *Biol. Soc. Wash. Bull.* **6**, 453 (1985).
17. S. K. Juniper, V. Tunnicliffe, A. R. Fontaine, *NOAA Natl. Undersea Res. Prog. Res. Rep. 88-4* (1988), p. 99.
18. S. K. Juniper, J. A. J. Thompson, S. E. Calvert, *Deep-Sea Res.* **33**, 339 (1986).
19. D. R. Janecky and W. E. Seyfried Jr., *Geochim. Cosmochim. Acta* **48**, 2723 (1984).
20. M. K. Tivey and R. E. McDuff, *J. Geophys. Res.* **95**, 12617 (1990).
21. U. M. Graham, G. J. Bluth, H. Ohmoto, *Can. Mineral.* **26**, 487 (1988).
22. T. L. Cook, thesis, University of California, Santa Cruz (1994).
23. R. A. Berner, in *Princeton Series in Geochemistry*, H. D. Holland, Ed. (Princeton Univ. Press, Princeton, NJ, 1980), pp. 90–126.
24. G. R. Taylor, *Mineral. Deposita* **18**, 129 (1983).
25. R. A. Berner, *Econ. Geol.* **64**, 383 (1969); R. E. Sweeney and I. R. Kaplan, *ibid.* **68**, 618 (1973); U. M. Graham and H. Ohmoto, *Geochim. Cosmochim. Acta* **58**, 2187 (1994).
26. J. N. Valette-Silver, A. Bates, D. Anderson, J. Deming, W. H. Zoller, *Eos* **66**, 97 (1985).
27. J. B. Murowchick and H. L. Barnes, *Geochim. Cosmochim. Acta* **50**, 2615 (1986).
28. R. M. Haymon, *Nature* **301**, 695 (1983).
29. Evidence for chalcopyrite replacement of wurtzite [atoll textures and disseminated chalcopyrite inclusions or "chalcopyrite disease" (*2*)] was observed in some of the structures.
30. We thank the Alvin and Atlantis II crew for assistance in obtaining these samples. Z. Palacz assisted with isotopic analyses, J. Delaney supplied unpublished location maps of the Endeavour structures, A. Gough assisted with figures, and J. Deming, J. Gill, M. K. Tivey, L. D. Abbott, and two anonymous reviewers provided helpful reviews. Support for this project was provided by the Monterey Bay Aquarium Research Institute with funds from the David and Lucille Packard Foundation. The cruise to obtain these samples was funded by the National Science Foundation.

7 September 1994; 23 December 1994

Atmospheric Methyl Bromide (CH_3Br) from Agricultural Soil Fumigations

K. Yagi, J. Williams, N.-Y. Wang, R. J. Cicerone*

The treatment of agricultural soils with CH_3Br (MeBr) has been suggested to be a significant source of atmospheric MeBr which is involved in stratospheric ozone loss. A field fumigation experiment showed that, after 7 days, 34 percent of the applied MeBr had escaped into the atmosphere. The remaining 66 percent should have caused an increase in bromide in the soil; soil bromide increased by an amount equal to 70 percent of the applied MeBr, consistent with the flux measurements to within 4 percent. Comparison with an earlier experiment in which the escape of MeBr to the atmosphere was greater showed that higher soil pH, organic content and soil moisture, and deeper, more uniform injection of MeBr may in combination reduce the escape of MeBr.

There is great interest (*1*) in quantifying how much of the stratospheric ozone loss observed to date is due to catalytic destruction by gaseous Br and BrO, and in predicting how future ozone amounts will respond to a decreased usage of anthropogenic organic bromine compounds (denoted by R-Br). Br atoms are carried into the stratosphere in relatively stable R-Br molecules such as the halons (principally $CBrF_3$ and $CBrClF_2$) and CH_3Br (MeBr). The fluxes of halons are known reasonably well as they are totally synthetic (*2*), whereas the rates of emission of MeBr into the atmosphere are poorly quantified. Even the atmospheric amounts of MeBr have been known only to within a factor of 2 until recently (*3*).

Two potentially significant sources of atmospheric MeBr have been recognized recently: emissions from large-scale biomass burning (*4*) and emissions from automobiles that burn leaded gasoline (*5*). Oceanic emissions have been considered a large natural source of MeBr, but recent data indicate that the oceans may be a net sink, not a source (*6*). Losses to the atmosphere during MeBr soil fumigations were recognized earlier but have not been well quantified. Model calculations show that MeBr escape from fumigated soils may be variable, depending on several factors (*7*). Whatever the putative sources, their total size, S, is constrained by $S = B/\tau$, where B is the atmospheric burden and τ is the atmospheric residence time, in an assumed steady state. Estimates of τ have changed recently from 2.0 to 1.3 years (*8*), and it is not clear that the sources identified to date can sum to $S = 1.4 \times 10^8$ kg/year (1.8×10^8 kg per 1.3 years). Constructing a budget of atmospheric MeBr requires more precise data.

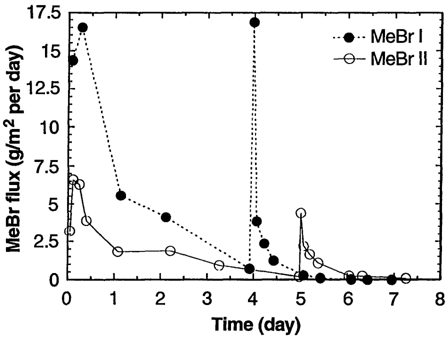

Fig. 1. Escape fluxes of MeBr measured with chambers placed over fumigated fields in two experiments near Irvine, California: MeBr I, 10 to 17 September 1992 and MeBr II, 8 to 15 October 1993. Data points are averages over all flux chambers (n = 5 in MeBr II and n = 4 in MeBr I). Polyethylene sheets covered the fields for 4 days in MeBr I and for 5 days in MeBr II. Standard deviations of the points for MeBr II varied between 8 and 27% of the means; the full range of variation for MeBr I was shown in (*9*).

Worldwide usage of synthetic MeBr increased from 4.2×10^7 to 6.3×10^7 kg/year between 1984 and 1990; about 80% of this amount was applied to agricultural soils before planting (*7*). MeBr may be removed from soils by hydrolysis, by adsorption to soil particles, by biological and chemical processes, and by transport. The rates and effectiveness of these varied processes have been shown, through modeling, to control the fraction of applied MeBr that escapes during soil fumigations (*7*). It is important to determine this escape fraction in actual fumigations and to identify the factors that control this escape so that they might be manipulated to minimize emissions.

We conducted a field fumigation experiment in which we measured the flux of MeBr into the atmosphere, the bromide contents of the soil before and after the experiment, and the gaseous MeBr in the soil versus depth. Measurement methods and other experimental details were those of Yagi *et al.* (*9*) except for the following modifications. The MeBr-chloropicrin mixture (75/25 by weight) was injected more uniformly than in (*9*) by a computer-controlled system, at a rate of 323 kg/ha (*10*). Plastic tarping was placed over the field immediately after the MeBr injection as described in (*9*), but it was left in place for 120 hours instead of 96 hours (*11*). We measured the fluxes by observing increases of MeBr gaseous concentrations in five flux chambers that were placed on top of the tarp, and after the tarp was removed, directly on the soil as described in (*9*). Soil gas concentrations of

---

K. Yagi, National Institute of Agro-Environmental Science, Tsukuba, Ibaraki 305, Japan.
J. Williams, N.-Y. Wang, R. J. Cicerone, Department of Earth System Science, University of California, Irvine, CA 92717-3100, USA.

*To whom correspondence should be addressed.